https://dx.doi.org/10.1016/j.addma.2023.103406

Development of conformal shell lattices via laser powder bed fusion and unraveling their mechanical responses via modelling and experiments

Jin Fu[a], Junhao Ding[b], Lei Zhang[c, d], Shuo Qu[b], Xu Song [b,*], M.W. Fu[a,**]

[a] Department of Mechanical Engineering, Research Institute for Advanced Manufacturing, The Hong Kong Polytechnic University, Hung Hom, Kowloon, Hong Kong, China

[b] Department of Mechanical and Automation Engineering, Chinese University of Hong Kong, Shatin, Hong Kong, China

[c] Department of Mechanical and Aerospace Engineering, Hong Kong University of Science and Technology, Clear Water Bay, Kowloon, Hong Kong, China

[d] Meta Robotics Institute, Shanghai Jiao Tong University, Shanghai, China

Email address: xsong@cuhk.edu.hk (Xu Song), mmmwfu@polyu.edu.hk (M.W. Fu).

Abstract

Additive manufacturing offers new design opportunities in employing lattice structures for lightweight applications. Especially, conformal lattice design can be made with internal lattice core with freeform external geometry. However, the mechanical response of conformal lattices is not well understood. In this work, triply periodic minimal surface (TPMS) based conformal shell lattices were designed based on isoparametric transformation method and fabricated by laser powder bed fusion (LPBF) to study the influence of key design factors on the mechanical properties of the conformal shell lattices. The results show that the deformation mechanism and mechanical properties of the shape-transformed structures are highly influenced by design factors including shape transformation type, tilting angle of side walls and cell orientation. The boundary between the misaligned shape-transformed TPMS does not deteriorate the mechanical properties and the energy absorption capability. Finally, conformal TPMS-filled monoclastic lattice was studied to verify the effectiveness of the conformal design for mechanical applications. It is found that the conformal TPMS-filled monoclastic lattice shows better mechanical performance than the uniformly in-filled counterparts. This work provides the first quantitative correlation between the design factors and the mechanical properties of the shape-transformed structures and highlights the potential of TPMS-based conformal design for real-world lightweight applications.

Keywords: triply periodic minimal surface, conformal shell lattices, isoparametric transformation, laser powder bed fusion, mechanical response.

1. Introduction

Cellular structures are gaining increasing attention and remarkable interests for its wide applications in different industrial clusters including light-weighting design, heat exchanger, tissue engineering and energy absorption [1]. Conventional manufacturing techniques, such as particle leaching and gas forming [2], is unable to fabricate desirable porous structures, as the produced structures often exhibit unpredictable and uncontrollable pore shape and size distribution, leading to unsatisfactory performance of the final products. Additive manufacturing (AM) technology has shown its unparalleled advantages with its ability to fabricate complex geometrical structures with short lead-time [3, 4]. The advancement of AM technology combined with powerful computer-aided design (CAD) methods offers great design freedom to create and fabricate satisfactory porous structures with freeform external shape and architected internal structures [3].

Architected cellular structures are usually designed with periodic porous unit cells, which can be categorized into strut-based, plate-based lattices and shell-based structures [5]. Although the strut-based lattice structure is the most investigated cellular structure so far, it could suffer from high stress concentration due to discontinuous strut junction under loading [6]. In addition, it may encounter manufacturability problem when the inclination angle of the strut is too low. For plate-based lattice structure, it possesses higher stiffness than that of strut-based lattice structure [7], but manufacturing of this type of structures remains a problem for powder-based AM systems due to the difficulty of powder removal. In recent years, triply periodic minimal surface (TPMS), a type of shell-based structure, has attracted great interest in industrial and academic areas. Compared with strut-based and plate-based lattice structures, TPMS structures can overcome the stress concentration problem with smooth curvature and continuous surface elements, and attain good manufacturability by AM [8]. In addition, the smooth surfaces could promote bone growth due to the structural similarity to natural trabecular bone, thus they have been considered as the most promising lattice structures for biomedical implants [9-12]. Moreover, TPMS structures exhibit greater specific energy absorption capability than strut-based structures with similar porosity [13, 14]. These advantages of TPMS structures are very attractive for biomedical, automotive and aerospace applications.

Designing externally freeform components with TPMS internal architectures can be achieved

via Volumetric Distance Field (VDF) based Boolean operations [15-18]. VDF is a 3D distance field defined within a rectangular domain. Each node in a VDF maps its minimum distance to the shape. VDF is used together with Boolean operations between two solid models A (external freeform shape) and B (internal TPMS structure). By extracting the resulting solid model from the operation (i.e., intersection: $\Phi(A) \cap \Phi(B)=\min(\Phi(A), \Phi(B))$), the regular TPMS structures with freeform external shapes can be created. Functional gradient and hybridization can be used concurrently to modify the internal TPMS structure [15], which aims to match the local porosity values for bio-scaffolding applications. However, this method only creates non-conformal TPMS core structures, which are oriented and positioned independently with the geometric form of the exterior surface. Using this method, the TPMS unit cells on the freeform boundaries usually have an incomplete structure with truncated surfaces, which result in weakened structure with low strength and stiffness [19]. Besides, the intersection operation of the external model and the internal TPMS structures is very expensive numerically and prone to error. On the contrary, the conformal TPMS structures can be oriented in accordance with the geometric form of the exterior surface, which not only preserves the local cell orientation, but also maintains the boundary cell integrity, resulting in the enhancement of mechanical properties. By using the isoparametric transformation of finite element method, Yoo [15] also proposed that the TPMS unit cells can be conformally mapped into arbitrary hexahedral elements while keep the continuity between adjacent elements. With this method, a component with freeform external shape and pre-meshed hexahedral elements can be infilled with integral TPMS structures. Kim and Yoo [20] also introduced a hybrid design method by combining a modified VDF-based Boolean operations and TPMS-based channel topologies to design arbitrarily shaped heat exchangers with conformal TPMS lattice cores. Combined with topology optimization, Zhao et al. [21] infilled the functionally graded sheet-based BCC lattices continuously and conformally into a design case of a pillow bracket with optimized volume fraction distribution. Conformal lattice components can also be created using some commercial software systems such as nTopology, which uses field-driven design approach [22]. For nTopology, the CAD geometries, meshes, planes, and points are all represented as distance fields [22]. However, current literature and the commercial software systems are generally focused on the geometry design of conformal lattice structures. There is a lack of study on the quantitative relationship between the design factors and the mechanical properties of the conformal lattices, as well as the understanding on the deformation mechanism of the conformal lattices, which is thereby the focus in this work. The superiority of the conformal lattice design over the uniform lattice is also rarely quantitatively revealed.

Upon establishment of a full database, these quantitative relationships could be implemented in the implicit design algorithm to automatically generate the conformal lattices structures with expected behaviors and properties.

In this work, we adopt the concept of isoparametric transformation in finite element method to generate conformal TPMS structures, in which integral TPMS unit cells are mapped into arbitrary hexahedral brick element. Extensive finite element (FE) modeling studies are conducted to study the deformation behavior and mechanical properties of the TPMS-based conformal lattices. Metallic TPMS specimens are fabricated by laser powder bed fusion (LPBF) of stainless steel 316L powder. Quasi-static compression experiments of the as-printed lattices are conducted to validate the FE models. The key design factors of the unit cell orientation, shape transformation and connection between cells are evaluated. Quantitative relationships between the key factors and the mechanical properties of the structures are analyzed. Finally, conformal and regular TPMS lattice infilled components were designed and tested to validate the superior crashworthiness of conformal lattice design. This work provides a valuable insight into designing conformal TPMS components for real-world applications.

2. Numerical and experimental methods

2.1 Geometrical modeling of conformal TPMS structures

The implicit design method for generating the conformal TPMS structure is described as follow. Step 1: Obtain the target geometry that TPMS needs to infill. It should be a 3D solid file that can be meshed by hexahedral elements; Step 2: Conduct the meshing and obtain the mesh file with node locations and element connection information as the input for the transformation and assembly step; Step 3: Choose the original regular TPMS structure type and rotate it to the preferred orientation based on the design requirement; Step 4: Conduct the isoparametric transformation of coordinates for each cell/element of the TPMS structures; Step 5: Assemble these cells/elements into the target geometry based on the mesh input file. Fig. 1 provides the flowchart of such process, with the TPMS structure mapped from a regular cell with different orientations ([100], [110] and [111]) to an arbitrary hexahedral cell and assembles them to a monoclastic geometry part. The regular TPMS lattice can be generated using the first-order approximation of the level set nodal equations. The formula of the study case of the Diamond (D-type) TPMS can be expressed as:

$$\emptyset_D = \sin(wx)\sin(wy)\sin(wz) + \sin(wx)\cos(wy)\cos(wz) + cos(wx)sin(wy)cos(wz) + cos(wx)cos(wy)sin(wz) = c \quad (1)$$

where x, y, z are spatial coordinates, $w=2\pi/L$ and L is the side length of a unit cell. The level c controls the pore size of the TPMS unit cell. Matlab coding is conducted to visualize the TPMS lattices, which are composed of a series of triangular facets. The facets are then written following STL format to generate a 3D model of the lattice. In this research, the TPMS cell orientation, which is neglected in the design of conformal lattice structures in current literature, is considered and implemented in the design algorithm.

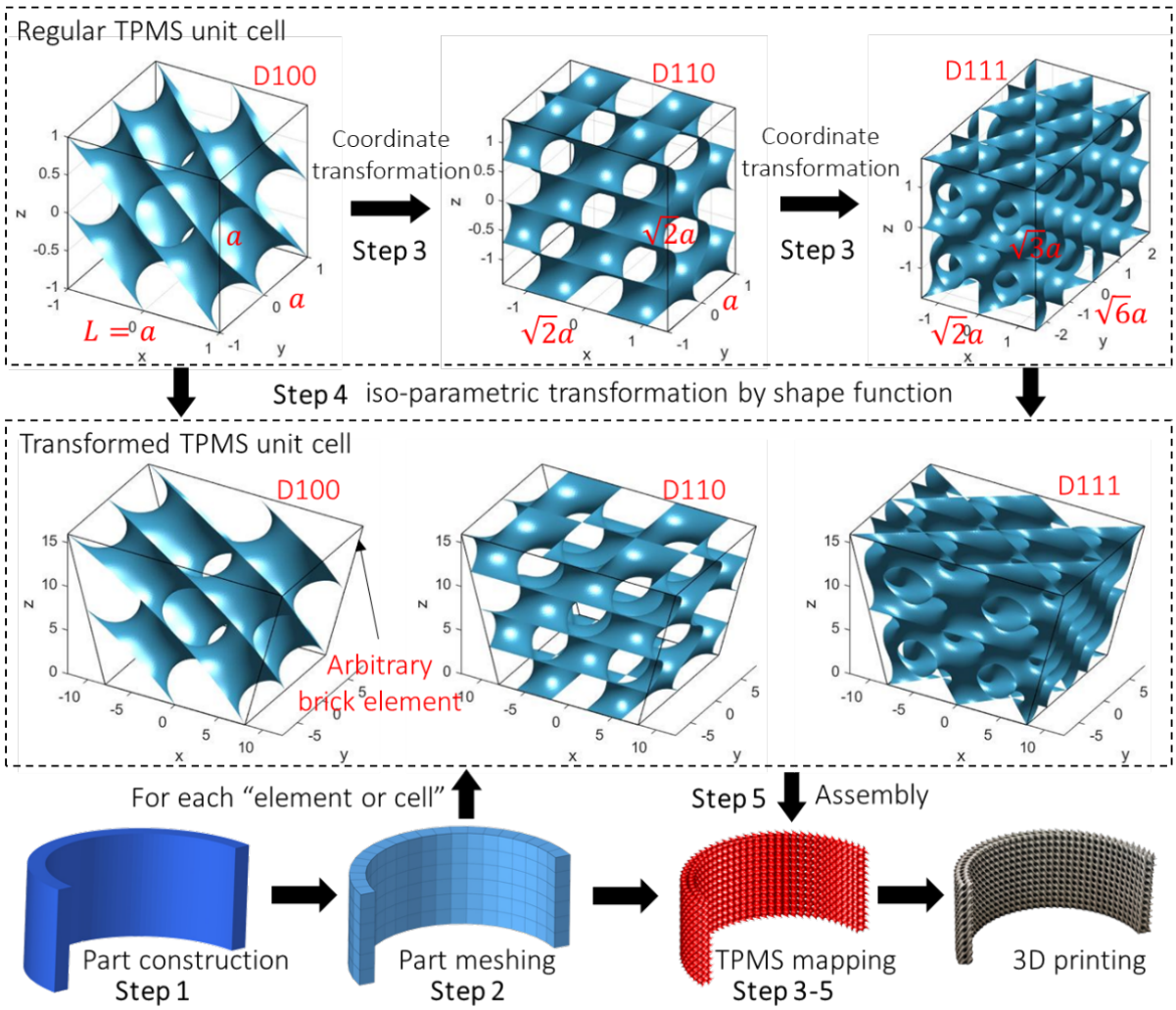

Fig. 1. Schematic diagram in generation of a component with conformal TPMS structure by iso-parametric transformation. Example is given using D-type TPMS unit cell to form a monoclastic component.

Further explanation of this method is provided below. For Step 1 and 2, the meshing is carried out in a mature commercial software Hypermesh, without the need to re-program the meshing algorithm. The mesh generated from this exercise can be made conformal in the software as well [23]. Such conformality in the mesh can be passed onto TPMS structures in the shape

function transformation later in Step 4 and 5. In Step 3, the generation of TPMS unit cell with orientations of [110] and [111] from the original [100] orientation is enabled by the coordinate transformation matrix $\boldsymbol{A}$, which is different for the three different cell orientations. The coordinate transformation matrix $\boldsymbol{A}$ can be obtained according to the face normal vectors of three different hexahedron unit cells as follows:

For [100] unit cell:

$$A_{[100]} = \begin{bmatrix} 1 & 0 & 0 \\ 0 & 1 & 0 \\ 0 & 0 & 1 \end{bmatrix} \tag{2a}$$

For [110] unit cell:

$$A_{[110]} = \begin{bmatrix} -1/\sqrt{2} & 0 & 1/\sqrt{2} \\ 1/\sqrt{2} & 0 & 1/\sqrt{2} \\ 0 & 1 & 0 \end{bmatrix}^{-1} = B_{[110]}^{-1} \tag{2b}$$

For [111] unit cell:

$$A_{[111]} = \begin{bmatrix} 1/\sqrt{2} & 1/\sqrt{6} & 1/\sqrt{3} \\ -1/\sqrt{2} & 1/\sqrt{6} & 1/\sqrt{3} \\ 0 & -2/\sqrt{6} & 1/\sqrt{3} \end{bmatrix}^{-1} = B_{[111]}^{-1} \tag{2c}$$

where the column vectors of the matrix $\boldsymbol{B}$ are the orthonormal vectors representing the face normals of the three different oriented parallelepipedic unit cells. [100]- and [111]-oriented TPMS structures can be obtained by operating the coordinate transformation matrix $\boldsymbol{A}$ on the coordinates on original [100] oriented TPMS. Furthermore, for successful mapping TPMS into components with multiple brick elements, TPMS unit cells that can be periodically arranged in the 3D space should be obtained to ensure the continuity in the interfaces between elements. In particular, the edge lengths are properly selected, namely $(\sqrt{2}a, a, \sqrt{2}a)$ for [110] oriented TPMS unit cell, and $(\sqrt{2}a, \sqrt{6}a, \sqrt{3}a)$ for [111] oriented TPMS unit cell [24], where a is the side length of original [100] TPMS unit cell, as shown in Fig. 1.

In Step 4 and 5, the isoparametric transformation idea is borrowed from the finite element method. With this transformation, we can map a regular TPMS structure in the local coordinates to the global Cartesian coordinates by iso-parametric interpolation, so that it can be "deformed" into a conformal cell/element. For example, considering a cubic tessellating cell of a TPMS represented by an eight-node hexahedral brick element, the shape functions of it are as follows:

$$N_i = \frac{1}{8}(1 + \zeta_i\zeta)(1 + \eta_i\eta)(1 + \varsigma_i\varsigma) \tag{3a}$$

$$x = \sum_i N_i x_i \;\; y = \sum_i N_i y_i \;\; z = \sum_i N_i z_i \tag{3b}$$

where (ζ, η, ς) are local coordinates. For the points located on a surface in the local coordinates with a mapping from a cubic element to an arbitrary hexahedral element, their coordinates in the global Cartesian system (*x, y, z*) are calculated by the interpolation in Eq. 3b, in which x_i, y_i, z_i are global Cartesian coordinates of hexahedral elements' vertices. Since the periodical TPMS unit cells with different orientations ([100], [110] and [111]) have different edge lengths, the original local coordinates (ζ', η', ς') should be normalized by each edge length, which guarantee successful mapping of unit cells with different orientations. Fig. 2 shows the steps of normalization of the local coordinates and operation of subsequent mapping.

Considering a TPMS with the STL format representation, which describes a surface by a series of triangular facets, the mapping can be done by calculating the Cartesian coordinates for each vertex of each triangle and the normal vectors based on these updated vertices. Conformal TPMS structure with preferred orientation can then be generated. Therefore, using the method proposed above, conformal TPMS structures in the STL format can be generated, which preserve the local TPMS cell orientation in a complex geometry. It is worth noting that the method above can only be viewed as a geometric modelling method for conformal TPMS structures. The detailed guideline for it to be used in the mechanical energy absorption area has not been discussed. Such information can only be revealed using a combined approach of FE simulation and quasi-static compression test in the following sections.

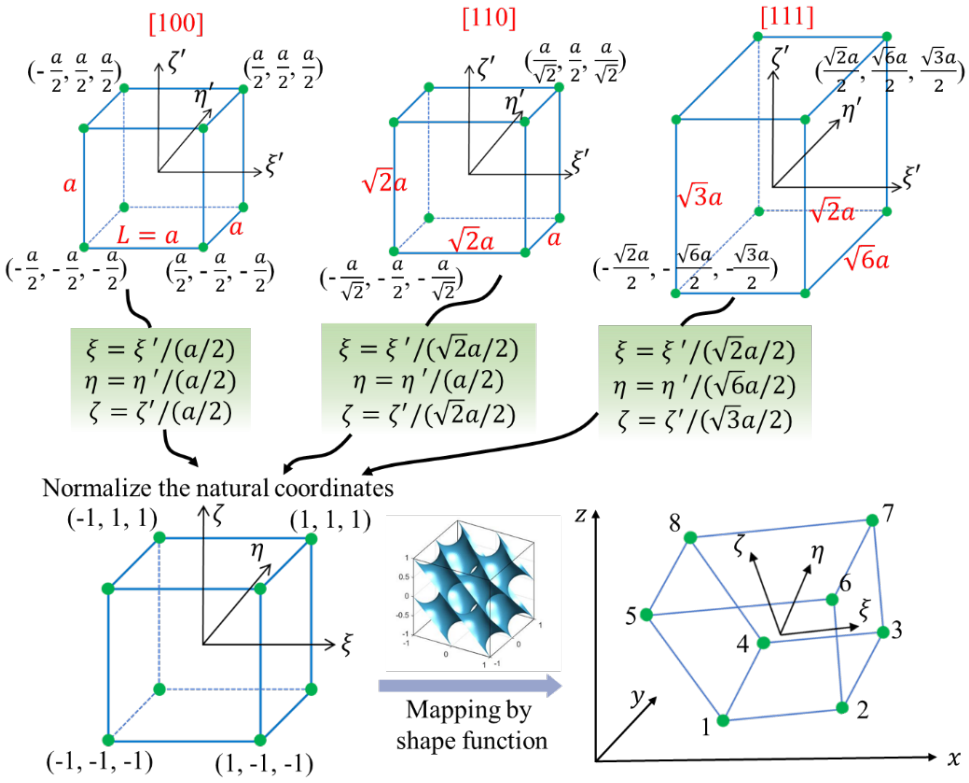

Fig. 2. Steps of normalization of the local coordinates and operation of subsequent mapping.

2.2 Finite element modelling

In this work, the key factors including shape transformation, unit cell orientation and cell connection were considered in FE modeling. Diamond-type TPMS structures were selected as the cases for FE modeling due to its superior mechanical properties comparing to other TPMS lattices [14, 25]. Three transformation types including monoclastic, synclastic and anticlastic types were studied. As shown in Fig. 3 (a), the monoclastic surface has a single curvature at a given point. The synclastic surface is curved to the same side along two directions, while anticlastic surface is curved convexly and concavely along two perpendicular plane sections. The individual hexahedral element with different side wall tilting angle is extracted for TPMS mapping (Fig. 3 (a)). The tilting angle refers to the angle between the tilted side wall of the transformed TPMS and the vertical direction. A5/A10/A15 represent the corresponding samples with tilting angles of 5/10/15°. To guarantee direct and valid comparison with the un-transformed TPMS, the mapped TPMS is cut so as to keep the same cubic shape and volume as the un-transformed one. The un-transformed TPMS is designated to contain 4*4*4 unit cells (a=4 mm in Fig. 1), which is able to provide properties close to the asymptote property of an infinite array [26]. Therefore, the designed TPMS cores with [100], [110] and [111] orientations along loading direction have dimensions of 16×16×16 mm^3,

$16\times16\sqrt{2}\times16\sqrt{2}$ mm^3, and $16\sqrt{6}\times16\sqrt{2}\times16\sqrt{3}$ mm^3, respectively. Similar method is applied for evaluating the connection between two transformed TPMS cells, as shown in Fig. 3 (b). Another connecting method by Sigmoid function is selected to benchmark the shape function method (Fig. 3 (c)). The connection of two misaligned TPMS by the Sigmoid function γ can be realized by the following expression:

$$\Phi_{connection} = \gamma\Phi_{TPMS1} + (1-\gamma)\Phi_{TPMS2} \quad (4a)$$

$$\gamma = \frac{1}{1+e^{kG(x,y,z)}} \quad (4b)$$

where $G(x,y,z)$ is a spatial coordinate set that describes the transition layer, and k defines the transition width. In this work, $G(x,y,z)$ represents the central vertical plane, and k=4 ensures a smooth transition at the boundary of about 3 mm in width. The example of two misaligned Primary TPMS connected by Sigmoid function is given in Fig. 3 (c).

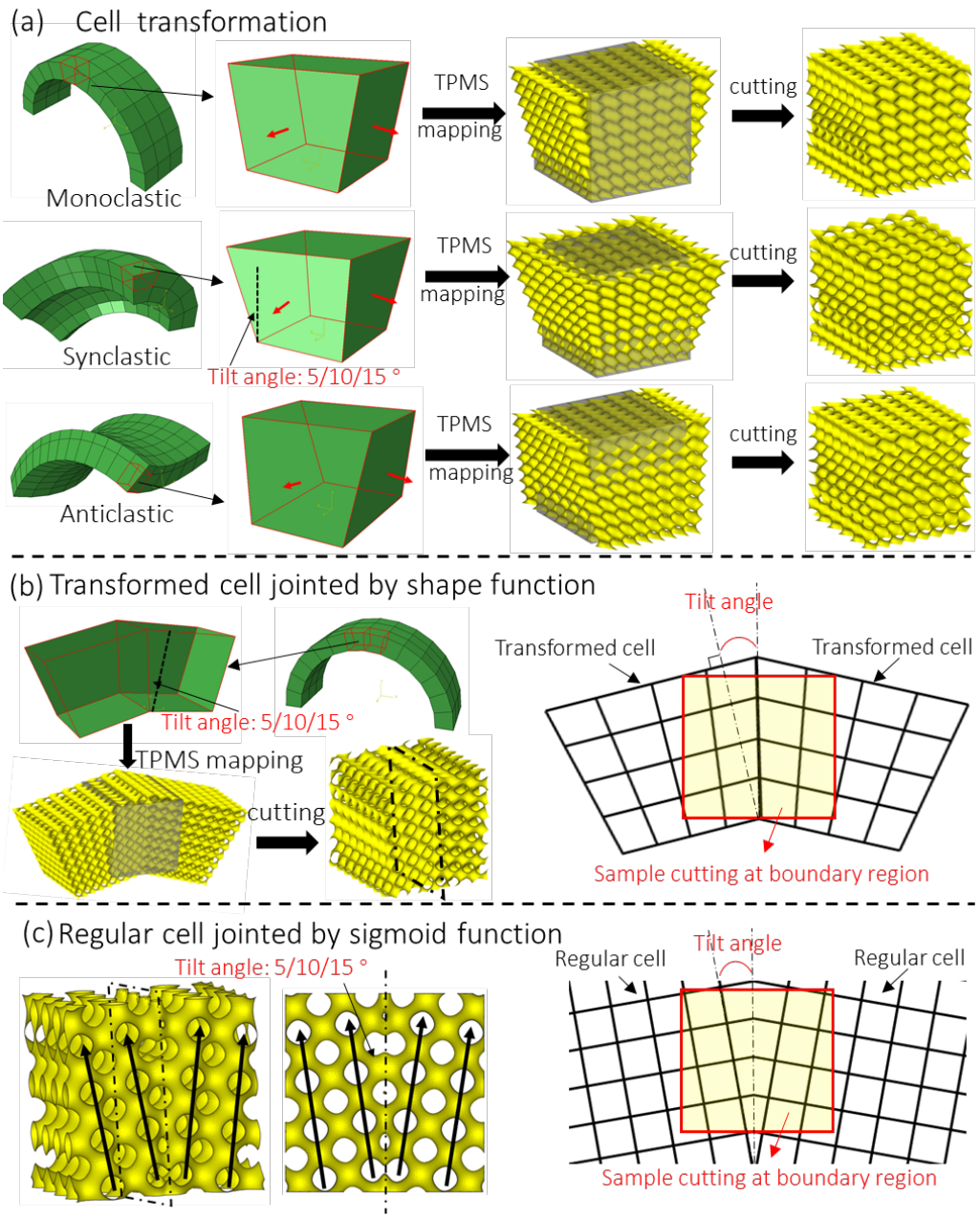

Fig. 3. TPMS sample preparation for FE modeling, additive manufacturing and subsequent evaluation: (a) cell transformation, (b) transformed cell jointed by shape function, (c) regular cell jointed by sigmoid function.

For FE modeling, the cubic TPMS models with shell element (S3) or triangular prism elements (C3D6) of average element size 0.2 mm were simulated, as shown in Fig. 4 (a). The element size of 0.2 mm was selected according to our previous work to balance the computational costs and analysis accuracy [27]. The TPMS cores in FE model were assigned with a certain shell thickness to keep the relative density at 10%. Other setups in the FE models including the material constitutive model (AMed SS316L) were the same as those in

our previous work [28]. Fig. 4 (b and c) shows the normalized stress-strain curves and the deformation modes during compression. Both C3D6 and S3 elements provide similar results in predicting the mechanical properties and the deformation mechanism of the TPMS structures with relative density around 10%, as shown in Fig. 4 (b and c). To save computation expense, S3 element was selected for FE modeling, which was also adopted in other studies [29].

For the case study in Section 3.3, FE modeling of 3-point bending of the cases were conducted to predict their crashworthiness. S3 element with average size of 0.1 mm was used since the unit lattice size is about half of the cubic TPMS models. The loading rate of the punch was 1mm/min, same as the experimental one. Other setups were same as those for cubic TPMS models.

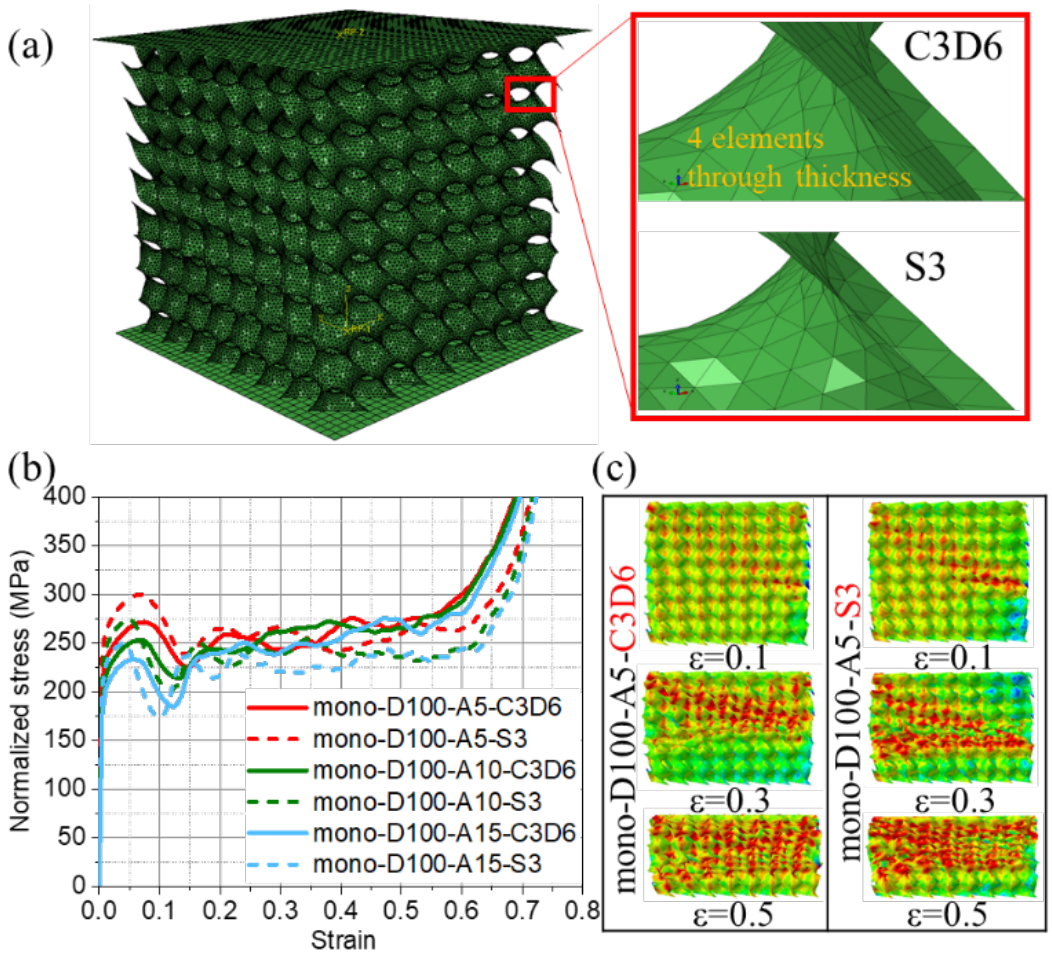

Fig. 4. (a) FE model of TPMS structure meshed with C3D6 and S3 elements, (b) FE simulated normalized stress-strain curves for mono-D100 type specimens, and (c) the corresponding stress distribution at three compressive strains.

2.3 Laser powder bed fusion of conformal TPMS specimens

The metallic powders of the ductile material SS316L with particle size ranging from 5-25 μm were purchased from Beijing AMC Powder Metallurgy Technology Co., Ltd for fabrication. The in-house developed micro LPBF system, which has been proven to enable high-precision manufacturing of complex structures [30], was adopted to fabricate the developed TPMS structures for further mechanical testing. The optimized process parameters including laser power of 50 W, scanning speed of 1000 mm/s, hatch spacing of 50 μm, and layer thickness of 10 μm were used [31].

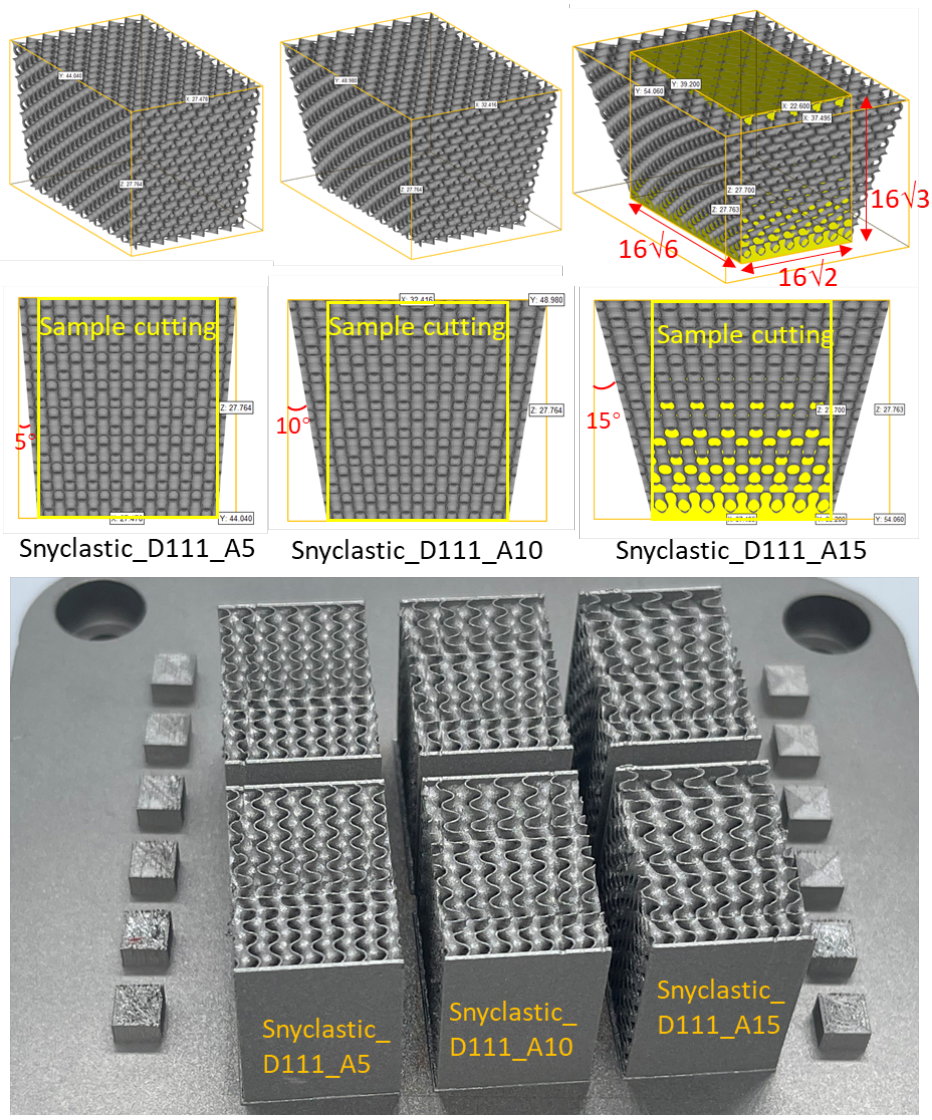

Fig. 5. Examples of the designed and as-printed synclastic D111 TPMS samples with different side wall tilting angles (5/10/15°).

A number of Diamond-type TPMS specimens were fabricated for validation of the FE models. All specimens were designed with a constant relative density of 10%, so the shell thickness could be different for different specimens due to different surface to volume ratios, as shown in Table 1. The designed TPMS cores with [100], [110] and [111] orientations along loading direction have dimensions of 16×16×16 mm^3, $16\times16\sqrt{2}\times16\sqrt{2}$ mm^3, and $16\sqrt{6}\times16\sqrt{2}\times16\sqrt{3}$ mm^3, respectively. As shown in Fig. 5, at least two specimens were fabricated for each type of TPMS structures. Two end plates with a thickness of 0.5 mm were added with the in-plane direction parallel to the building direction, aiming to avoid adding support structures and guarantee a load bearing plane that is parallel to the loading platform. The addition of end plates has a limited effect on the mechanical property of the TPMS if the sample contains enough number of unit cells [27]. The relative density was measured based on the dry weighing method in the same way as our previous work. Table 1 shows measured relative density of the as-printed Diamond-type TPMS specimens. Noted that the abbreviations "mono", "anti" and "syn" denote monoclastic, anticlastic and synclastic samples, respectively. "Jointmono" and "Sigmoid" denote the jointed specimens by shape function and Sigmoid function, respectively.

Table 1. Details of the 3D models and as-printed TPMS structures.

	TPMS type	Surface/volume (mm^{-1})	STL shell t (mm)	Measured ρ_r (%)
	Original D100/110/111	0.960/0.963/0.959	0.104/0.104/0.104	10.9/11.9/11.9
Cell transformation	Mono-D100-A5/A10/A15	0.941/0.922/0.906	0.107/0.109/0.111	12.1/12.8/13.0
	Anti-D100-A5/A10/A15	0.916/0.876/0.844	0.109/0.114/0.119	13.4/12.0/12.2
	Syn-D100-A5/A10/A15	0.916/0.881/0.843	0.109/0.113/0.119	13.6/14.2/13.9
	Syn-D110-A5/A10/A15	0.909/0.861/0.827	0.110/0.116/0.121	12.9/13.5/12.8
	Syn-D111-A5/A10/A15	0.920/0.881/0.848	0.109/0.114/0.118	12.4/13.0/12.1
Joint	Jointmono-D100-A5/A10/A15	0.929/0.897/0.873	0.108/0.112/0.115	12.7/13.4/14.0

Sigmoid-D100-A5/A10/A15	0.967/0.979/0.976	0.104/0.103/0.103	14.1/13.2/13.3

2.4 Quasi-static compression tests

Quasi-static compression tests of the as-printed cubic TPMS specimens were conducted on an MTS universal tester at a strain rate of ~10^{-3} s^{-1} and stopped after reaching densification. The deformation history of the specimens was recorded using a camera. Considering the good repeatability of LPBF and the compression testing results, the compression tests were repeated for two times for each kind of TPMS structures [27, 29, 32, 33]. The stress and the strain were calculated as the loading force divided by the cross-sectional area, and the crosshead displacement divided by the height of the TPMS cores, respectively. The engineering stress was normalized by the measured relative density. This is to eliminate the effect of the deviation of actual relative density between the various specimens, as shown in Table 1. Moreover, the stress normalization allows direct evaluation of the efficiency of different TPMS geometries. However, one should note the stress is over normalized since the measured relative density is higher than the effective relative density due to the existence of non-contributory adhered powders.

For the case study in Section 3.3, the crashworthiness of the cases was evaluated. The punch moved at a loading rate of 1mm/min up to a displacement of 6 mm. The deformation history of the specimens was also recorded using a camera. Identically, the test was repeated two times for each case. The experimental load-displacement curves were extracted for analysis of mechanical performance.

3. Results and discussion

3.1 Effects of design factors on deformation mechanisms

Figs. 6, 7 and 8 present the numerical and experimental stress-strain curves and deformation patterns of the shape-transformed and jointed TPMS structures. The normalized experimental (EXP) and numerical (FE) stress is calculated as the stress divided by the measured relative density and the ideal relative density (10%), respectively. The curves in black belong to the original D-type TPMS without shape transformation, which are used to benchmark the performance of the shape-transformed ones. In general, all of these EXP and FE specimens show a similar stress-strain behavior, including a linear elastic deformation region until

reaching the initial peak stress, a plateau region with stress fluctuation, and a final densification region with stress growing rapidly, as is reported in many other literatures on lattice structures [34-36]. It implies that FE models are generally valid to predict the mechanical performance of the as-printed TPMS specimens. However, the experimental stresses of the as-printed TPMS specimens are generally lower than that of the corresponding numerical ones. The over-prediction of stresses in numerical simulation is caused by simplification of the material constitutive behavior in numerical modelling and the AM defects [37]. The AM defects, including surface-adhered powders and internal pores or cracks, could lower the mechanical efficiency of the TPMS structures, i.e., the strength and energy absorption performance, which will be quantified in the next sections. On the other hand, the adhered powders increase the shell thickness and the measured relative density, leading to the lower normalized mechanical properties of the printed lattices. In future research, an accurate constitutive model of the AMed metals and alloys should be developed by considering these shortcomings, aiming at obtaining the accurate prediction of the mechanical performance of the AMed lattices. Despite of this, there is a good agreement between the experimental and numerical deformation patterns of the shape-transformed and jointed TPMS specimens. The numerical results also show the stress distribution within the structures during compression, which helps to understand the deformation mechanisms. The design factors have evident influences on the deformation mechanisms of the shape-transformed and jointed specimens, which will be discussed as follows:

3.1.1 Effect of tilting angle and transformation type

With increasing tilting angle, the monoclastic specimens have similar level of plateau region and slightly lower initial peak stress as the original one (Fig. 6 (a)), while evident lowered plateau region is observed for anticlastic specimens (Fig. 6 (c)). More interesting is the increasing slope of the plateau region for synclastic specimens (Fig. 7 (a)), suggesting a continuous hardening behavior during compression, especially for specimens with high tilting angle. In addition, the deformation patterns indicate that with increasing tilting angle, the deformation of monoclastic and synclastic specimens tends to be a layer-by-layer collapse of the horizontal layers from top to bottom, as shown in Figs. 6 (b) and 7 (b). In contrast, the collapse of anticlastic specimens with high tilting angle is featured by the double horizontal shear bands at the top and bottom regions (Fig. 6 (d)).

It can be easily understood through the tilting orientation of the side walls. For synclastic

specimens, the four side walls are all tilted towards the same direction, leading to a continuously increasing pore size from bottom to top, and thereby a gradient local relative density and load bearing capacity. Monoclastic specimens also have gradient features but not as evident as synclastic counterparts, since there is only one pair of side walls were tilted. As a result, the synclastic and monoclastic specimens with high tilting angle collapse layer by layer starting from the weak top region. In contrast, the two pairs of the side walls of anticlastic specimens have opposite tilting direction, as shown in Fig. 3 (a), which leads to lower relative density at both top and bottom regions as compared with middle region. Therefore, stress is highly concentrated at the two weak ends of TPMS cores and initiates plastic collapse.

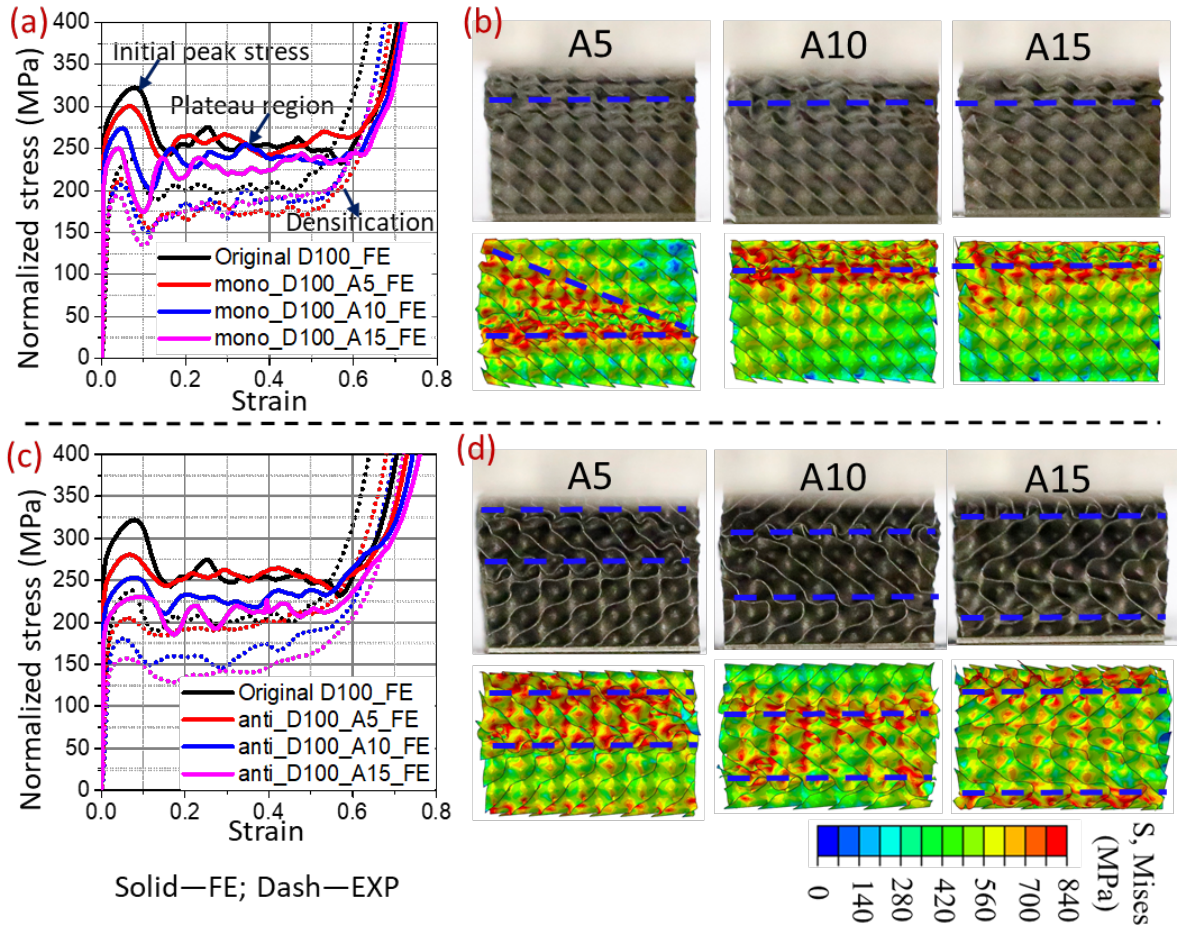

Fig. 6. Numerical and experimental (a, c) normalized stress-strain curves and (b, d) deformation patterns (at the strain of 0.3) of shape-transformed TPMS structures: (a, b) monoclastic_D100, (c, d) anticlastic_D100.

3.1.2 Effect of cell orientation

Similar as some solid metals [38], anisotropic stress-strain behavior is also detected for shape-transformed TPMS specimens. The synclastic specimens with [100] direction exhibit the highest initial peak stress and plateau stress. The counterparts with [111] orientations show a nearly periodic stress oscillation during plateau region, which is corresponding to the layer-by-layer collapse of the structures. Interestingly, it is found that the amplitude of the stress fluctuation is higher for the FE case than the EXP case, as shown in Fig. 7 (e and f). It is largely attributed to the adhered powers, which lead to an earlier (compared with the ideal FE case) contact of adjacent collapsed sublayers followed by the immediate collapse of the next sublayer.

Furthermore, the variation of the cell orientation slightly changes the deformation mode for transformed samples with smaller tilting angle (A5) but doesn't affect those with higher tilting angles (A10/A15), which deform in a layer-by-layer mode. That means the deformation mode is highly influenced by the tilting angle instead of the cell orientation, since the former could lead to significant variation of local relative density, hence the variation of the local load-bearing capacity.

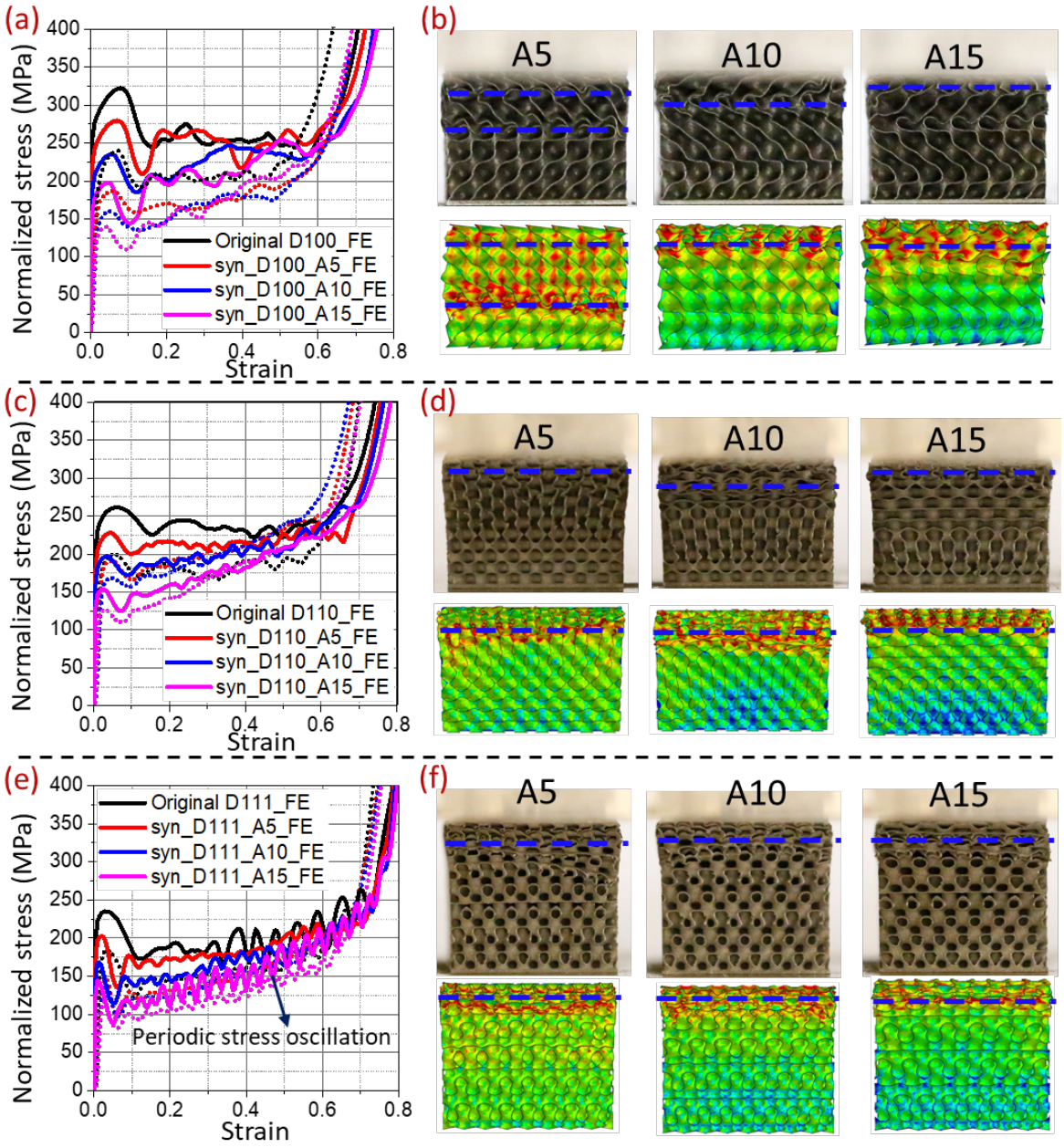

Fig. 7. Numerical and experimental (a, c, e) normalized stress-strain curves and (b, d, f) deformation patterns (at the strain of 0.3) of shape-transformed TPMS structures: (a, b) synclastic_D100; (c, d) synclastic_D110; (e, f) synclastic_D111. The color plots show the von Mises stress with the same color bar as shown in Fig. 6.

3.1.3 Effect of boundary between jointed cells

Fig. 8 shows the effect of the boundary on the compressive response of the jointed structures with misalignment. Comparing Figs. 8 (a) and 6 (a), it is found that the stress-strain behavior of the monojoint_D100 specimens is quite similar to that of the shape-transformed specimens, i.e., monoclastic_D100, in terms of the initial peak stress, the plateau region and the

densification point. It means that the boundary region does not behavior worse than other regions in conformal TPMS components. For the benchmark case in Fig. 8 (c), namely the misaligned regular TPMS connected by Sigmoid function, the numerical results present similar level of the plateau region for the three tilting angles (5/10/15°). In experimental cases, however, higher tilting angle (10/15°) results in a lower plateau region. In fact, the small tilting angle in specimens jointed by Sigmoid function can still ensure a relatively smooth transition at the boundary. With increasing misorientation, however, there are inevitably some sharp regions, which deteriorate the manufacturability and thereby the plateau strength.

Compared with the normal shape-transformed region (Mono-D100), the jointed regions (Jointmono-D100) exhibit similar deformation patterns during compression, i.e., shear band formation followed by layer-by-layer failure (A5), and layer-by-layer failure from top to bottom (A10 and A15). This suggests the boundary between the adjacent shape-transformed specimens can effectively attain a smooth transition without disturbing the continuity of the lattice structure and altering the deformation mode. In addition, for the benchmark case, it is found that the boundary created by the Sigmoid function significantly changes the original deformation mode. Particularly for high tilting angle (A10 and A15), the sublayer failure occurs at various regions within the structures simultaneously, which suggests the Sigmoid function cannot ensure a stable transition and is inefficient in cell connection.

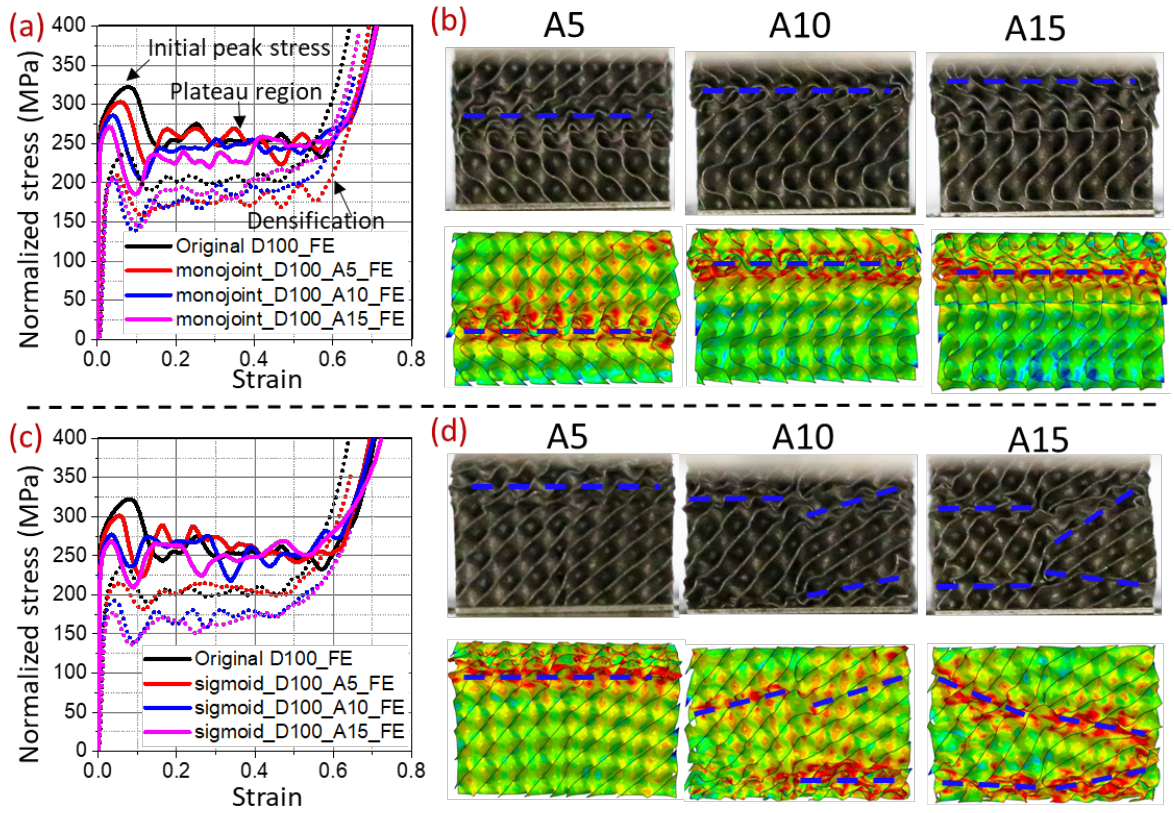

Fig. 8. Numerical and experimental results on (a, c) normalized stress-strain curves and (b, d) deformation patterns (at the strain of 0.3) of the jointed TPMS structures (a, b) by shape function and (c, d) by sigmoid function. The color plots show the von Mises stress with the same color bar as shown in Fig. 6.

In short, the deformation mechanism is highly influenced by the tilting angle of the side walls and the type of shape transformation, while the variation of cell orientation does not evidently change the deformation mode. Different shape transformation can realize different gradients of relative density within the structure. As a result, the shape-transformed TPMS could deform like a functional gradient structure, which have been well studied and presented in [39-44]. By tailoring the tilting angle, functionally graded TPMS-filled conformal components structures can be designed using the proposed design methods and AM techniques, and will be attractive in lightweight, stress tolerant and energy absorbing applications. In addition, the results also reveal that large tilting angle should be avoided in conformal design to prevent excessive loss of mechanical properties. Moreover, the connection between misaligned TPMS structures by using isoparametric transformation is generally more effective than using Sigmoid function.

3.2 Effects of design factors on mechanical properties

This section aims to quantify the mechanical properties and energy absorption capacity of the transformed and jointed TPMS specimens. Following the standard ISO 13314:2011 [45], the plateau strength is calculated as the mean stress between 0.2 and 0.4 strain range. The energy absorption per volume (E) is calculated as the area under the stress-strain curve within the strain range of 0 to 0.5. In regard to the crashworthiness, some common indicators, including absolute energy absorption (W), specific energy absorption (SEA), average crushing force/stress (F_{av}/σ_{av}), maximum crushing force/stress (F_{max}/σ_{max}) and crushing efficiency (η), are used as the crashworthiness criteria [46]. In detail, the energy related indicators E and W can be expressed as:

$$E = \int_0^{\delta} \sigma(\varepsilon) d\varepsilon \tag{5}$$

$$W = \int_0^{d} F(x) dx \tag{6}$$

where δ is the strain (0.5 for cube specimens) and d is the corresponding displacement. SEA denotes the absorbed energy per unit mass of the structures and can be formulated as:

$$SEA = \frac{W}{m} = \frac{E}{\rho_r * \rho_m} \tag{7}$$

where m is the mass of the structures, ρ_r is the relative density, and ρ_m is the density of the solid material (7.98 g/cm^3 for SS316L). For FE model, the designed mass is used, while the measured value of as-printed structures is used for experimental SEA calculation. Evidently, a structure with higher SEA value possesses better energy absorption capability. In addition, the crushing efficiency, η, is also widely used to indicate the energy absorption capacity of a structure. Higher value of η indicates more efficient structure design for energy absorption. η is calculated as:

$$\eta = \frac{F_{av}}{F_{max}} \times 100\% = \frac{\sigma_{av}}{\sigma_{max}} \times 100\% \tag{8}$$

where the average crushing force, F_{av}, is expressed as:

$$F_{av} = \frac{W}{d} \tag{9}$$

Fig. 9 and 10 show the mechanical properties including the normalized initial peak strength, plateau strength and energy absorption performance of the shape-transformed and jointed TPMS structures. Table 2 shows the extracted statistics of the mechanical properties. It should be noted that the trend of specific energy absorption (Fig. 10) is consistent with the plateau strength (Fig. 9). Both numerical and experimental results show similar trend, namely, the

overall mechanical properties decrease with increasing tilting angle. It implies that an appropriate tilting angle should be selected to avoid excessive loss of mechanical properties. In detail, for monoclastic specimens (see Fig. 9 (a) and Fig. 10 (a)), the slopes of the decreasing initial peak strength, plateau strength and energy absorption as the function of tilting angle are the smallest compared with other shape-transformed specimens, which is associated with the minimum local relative density within the structure. For anticlastic specimens in Fig. 9 (b) and Fig. 10 (b), it can be found that the actual and predicted strength and energy absorption property present almost the same trends. For synclastic D100/D110/D111 specimens, the predicted mechanical properties obey the following sequence: synclastic D100>D110>D111, which is same as the original D-type TPMS (see A0 data). This indicates that the transformed TPMS maintains the anisotropy of mechanical properties as the regular TPMS. Interestingly, the experimental plateau strength suggests different or even reversed trends compared with the predicted ones, see the green lines in Fig. 9 (c-e). The tested plateau strength for synclastic D110 is even higher than the original D110 TPMS (A0). In addition, both numerical and experimental plateau strength (green lines) are comparable or even higher than the corresponding initial peak strength (orange lines) at high tilting angles (A10/A15). These phenomena are also related to the functional gradient structure realized by the shape transformation, and the adhered powders which promote earlier contact of sublayers during compression and enhance the plateau strength.

Fig. 9 (f, g) and Fig. 10 (f, g) shows the effect of connecting boundary on the mechanical properties of jointed TPMS specimens. By comparing with normal single monoclastic element (Fig. 9 (a) and Fig. 10 (a)), it is found that the mechanical properties and the energy absorption at the boundary region are almost the same as those of the normal region of monoclastic specimens. It again proves that the boundary between the connected shape-transformed TPMS dose not deteriorate the mechanical properties and the energy absorption capability. For misaligned specimens jointed by Sigmoid function (Fig. 9 (g) Fig. 10 (g)), it is found that the mechanical properties in the experiments deteriorate faster with increasing tilting angle, which could be attributed to the limited manufacturability of the sharp regions at the high-angle boundary.

It is interesting to find that the crushing efficiency of the shape transformed TPMS (red lines in Fig. 10) shows an increase at A5 condition compared with the original TPMS. This should be attributed to the functional gradient property induced by tilting of the side walls. However,

with increasing tilting angle, the crushing efficiency of the specimens present a significant decrease, which is due to the largely deteriorated mechanical properties. It suggests that the large tilting angle in conformal lattice designed based on the isoparametric transformation should be avoided. Alternative solutions, such as, refining the hexahedral elements of the 3D solid file, should be considered instead. In short, the mechanical properties including the energy absorption capability and efficiency of the shape-transformed and jointed misaligned TPMS specimens are controlled by the tilting angle, shape transformation type and cell orientation. To obtain desired mechanical properties, design of dedicated conformal TPMS components should consider the critical value of the tilting angle, the appropriate shape transformation type and the optimal cell orientation. In addition, with the aim to coordinate various design factors and develop precise design guideline for conformal TPMS components with desired mechanical performance, more comprehensive and efficient FE and EXP studies should be conducted by considering more TPMS types in the future work. The quantitative relationship between the design factors and mechanical properties contributes to the development of design guidelines for the conformal TPMS-filled components with the desired mechanical properties.

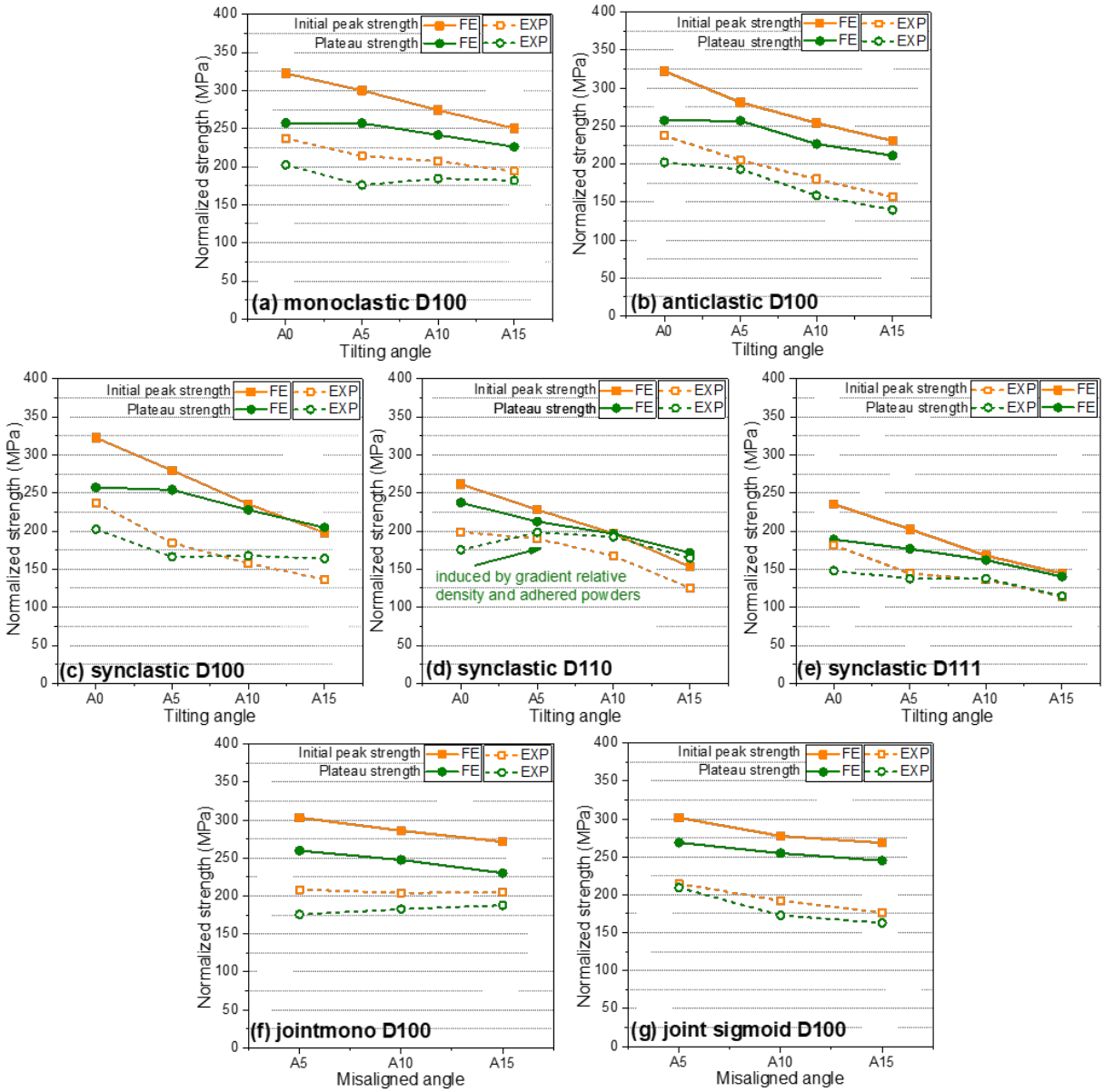

Fig. 9. Normalized initial peak strength and plateau strength of the shape-transformed and jointed TPMS specimens: (a) monoclastic D100, (b) anticlastic D100, (c) synclastic D100, (d) synclastic D110, (e) synclastic D111, (f) joint-mono D100 and (g) joint-sigmoid D100.

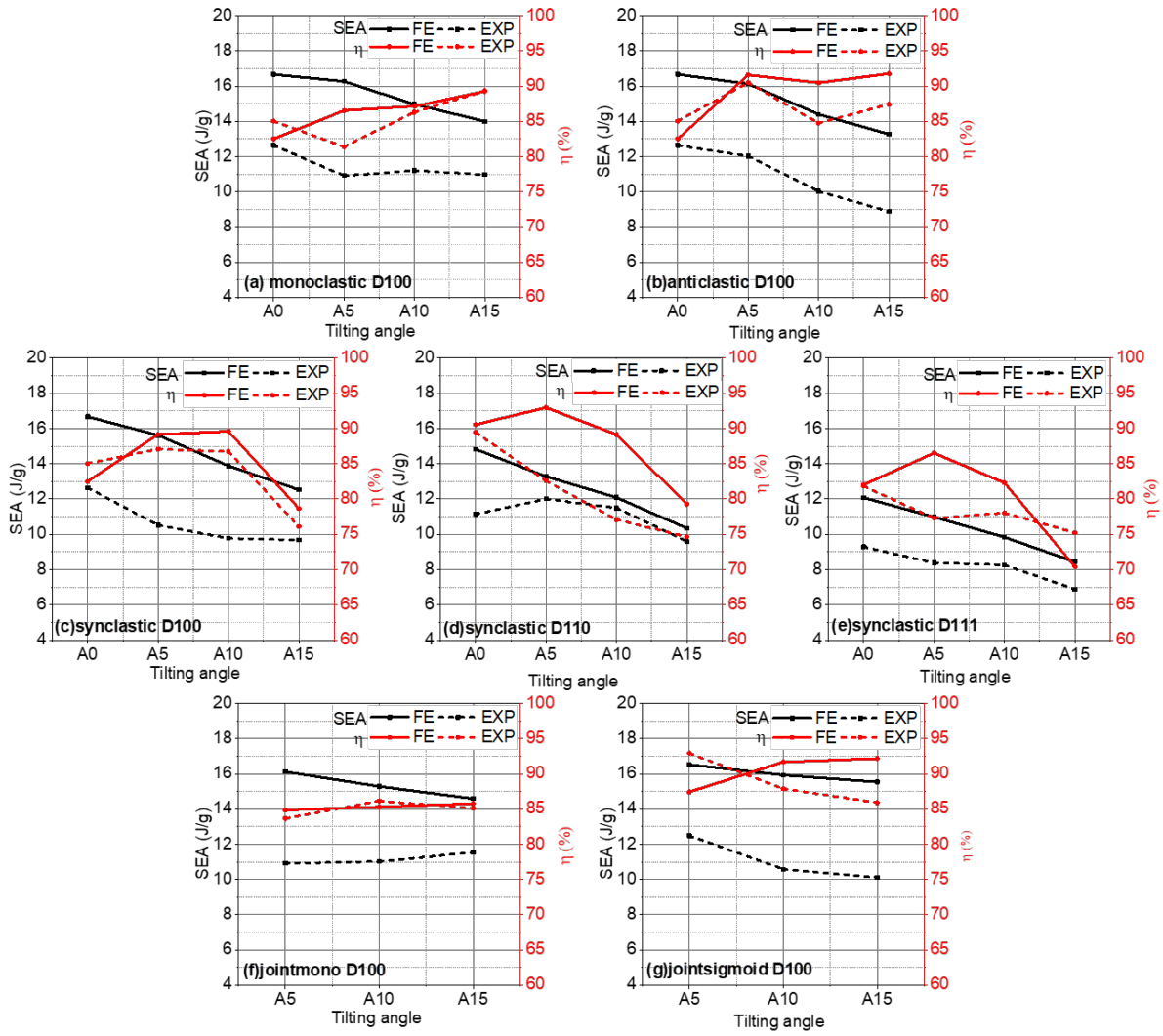

Fig. 10. Specific energy absorption and crushing efficiency of the shape-transformed and jointed TPMS structures: (a) monoclastic D100, (b) anticlastic D100, (c) synclastic D100, (d) synclastic D110, (e) synclastic D111, (f) joint-mono D100 and (g) joint-sigmoid D100.

Table 2. Mechanical properties of the shape-transformed and jointed TPMS structures

Specimens		Initial peak strength		error	Plateau strength		error	Specific energy absorption		error	crushing efficiency		error
		FE	EXP		FE	EXP		FE	EXP		FE	EXP	
D100		322.39	237.15	26.44	257.32	202.20	21.42	16.67	12.64	24.18	82.51	85.04	2.98
D110		261.39	198.68	23.99	237.25	175.27	26.12	14.83	11.14	24.92	90.56	89.45	1.22
D111		235.11	181.17	22.94	188.96	147.88	21.74	12.08	9.29	23.14	82.03	81.83	0.25
mono-D100	A5	299.97	214.04	28.65	257.02	175.80	31.60	16.27	10.91	32.90	86.54	81.39	5.95
	A10	274.18	207.07	24.48	241.46	184.26	23.69	14.97	11.20	25.20	87.14	86.31	0.95
	A15	250.27	193.74	22.59	225.92	181.69	19.58	14.00	10.97	21.64	89.28	89.33	0.06
anti-D100	A5	281.12	204.91	27.11	256.88	193.08	24.83	16.13	12.02	25.51	91.59	90.50	1.19
	A10	254.02	180.24	29.04	226.46	158.65	29.94	14.40	10.03	30.37	90.48	84.75	6.33
	A15	230.70	156.54	32.15	211.19	139.66	33.87	13.27	8.87	33.16	91.78	87.44	4.73
syn-D100	A5	279.61	184.56	33.99	254.11	166.18	34.60	15.62	10.52	32.62	89.16	87.09	2.32
	A10	235.46	157.67	33.04	227.77	167.54	26.44	13.88	9.77	29.65	89.60	86.74	3.19
	A15	197.85	136.61	30.95	204.71	164.00	19.89	12.52	9.68	22.65	78.67	76.11	3.25
syn-D110	A5	227.92	189.93	16.67	212.46	198.29	6.67	13.28	12.01	9.58	92.97	82.60	11.15
	A10	196.96	167.38	15.02	196.40	192.33	2.07	12.09	11.50	4.89	89.15	77.07	13.54
	A15	153.13	125.02	18.36	171.45	164.44	4.09	10.34	9.60	7.13	79.26	74.65	5.82
syn-D111	A5	202.45	144.27	28.74	176.55	137.53	22.10	10.98	8.38	23.62	86.53	77.29	10.67
	A10	167.78	136.03	18.92	161.83	137.47	15.05	9.84	8.26	16.03	82.30	78.03	5.19
	A15	144.30	113.90	21.07	140.25	114.74	18.18	8.44	6.89	18.35	70.44	75.23	6.36
jointmono-D100	A5	303.21	208.32	31.30	259.75	175.51	32.43	16.12	10.92	32.25	84.85	83.67	1.38
	A10	285.99	204.09	28.64	247.60	182.60	26.25	15.29	11.02	27.93	85.31	86.15	0.98
	A15	271.37	204.77	24.54	230.22	187.70	18.47	14.59	11.54	20.90	85.78	85.11	0.79
jointsigmoid-D100	A5	301.57	214.56	28.85	268.88	209.41	22.12	16.52	12.49	24.38	87.44	92.94	5.92
	A10	277.29	192.18	30.69	254.77	172.97	32.11	15.93	10.58	33.56	91.69	87.89	4.14
	A15	268.57	176.71	34.20	245.04	162.92	33.51	15.54	10.11	34.98	92.19	85.91	6.81

3.3 Effectiveness of conformal TPMS components for energy absorption applications

3.3.1 Conformal TPMS-filled monoclastic lattice

For the components with complex geometries, if filling the component with the original TPMS, sharp edges and unintegral unit cells are inevitable, which could deteriorate the mechanical performance. In contrast, the conformal design can align the lattice orientations with the curvature directions of the macroscopic structure and maintain the TPMS integrity at the structural boundaries, which is expected to show a better mechanical performance over the uniform TPMS-filled component. To manifest the superiority of TPMS lattice structures, a simple component with monoclastic surface is proposed as the case study to evaluate the effectiveness of the conformal lattice components for energy absorption applications. Such a monoclastic lattice structure can be used to absorb mechanical energy in such a way to protect

the important internal components. Fig. 11 (a) shows the procedure for design of the conformal TPMS-filled monoclastic lattice structure by using the iso-parametric transformation as introduced in Section 2.1. To fully leverage the advantage of the conformal design, the unit cell direction [100], which offers the best mechanical properties of D-type TPMS, is aligned along the normal direction of the monoclastic surface via shape transformation. In addition, the structure filled with the uniform TPMS is designed as a comparison case, as shown in Fig. 11 (b). To enable the results to be comparable, the cell size of uniform TPMS is 5 mm, which is the same as the size of C3D8 element for conformal design. The compression performance of the two cases was experimentally and numerically evaluated, as shown in Fig. 11 (c). The same LPBF process configurations are used to manufacture the lattices for evaluation of the manufacturability and properties of the samples. The as-printed lattices are shown in Fig. 11 (d).

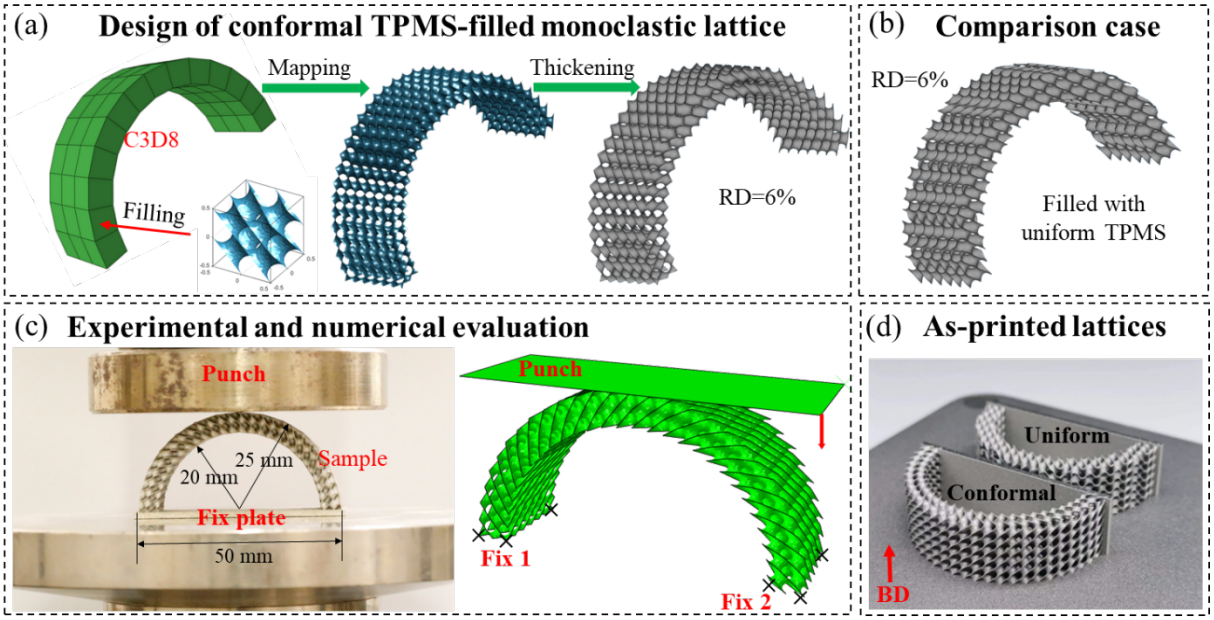

Fig. 11. (a) The procedure for design of the conformal TPMS-filled monoclastic lattice; (b) comparison case of uniform TPMS-filled monoclastic lattice used for benchmarking; (c) setups of experimental and numerical evaluation of compression performance of the lattices; (d) the as-printed lattices.

3.3.2 Mechanical performance of the TPMS-filled monoclastic lattices

The crashworthiness of the conformal and uniform TPMS-filled monoclastic lattices is numerically and experimentally evaluated by compression test. Fig. 12 (a) shows the numerical and experimental load-displacement curves of the two cases. The deformation

starts with an elastic region, followed by a softening region, where the lattices experience a plastic collapse. Both numerical (FE) and experimental (EXP) curves reveal that the conformal TPMS-filled lattice has a better compression performance. Fig. 12 (b) shows the simulated stress distribution and the experimental deformation pattern. Specifically, the uniform case suffers a more severe stress concentration compared with the conformal case, which should be attributed to the sharp edges of the unintegral TPMS unit cells and the resultant non-uniform loading-bearing capacity.

Table 3 lists the various calculated crashworthiness criteria for conformal and uniform cases. Both simulated and experimental values suggest that the mechanical properties including the initial peak force, W, SEA and η of the conformal TPMS-filled monoclastic lattice are higher than that of the uniform case, suggesting the superiority of the conformal design. In detail, the experimental values show that the conformal case has a higher initial peak force ($F_{initial}$) with an increase of 18.7% compared with the uniform case. The specific energy absorption (SEA) of the conformal one is even 32% higher than that of the uniform one, as also illustrated in Fig. 12 (a). The SEA of the as-printed structures is smaller than the ideal value, which is attributed to the adhered powders, as shown in Fig. 12. It is possible to increase the SEA of the LPBFed structures by an appropriate surface post processing to improve the surface quality of the complex lattice structures, such as chemical etching and sand blasting [47-49]. In short, the conformal structures with integral unit cells can produce more desirable mechanical performance with a promising potential for lightweight applications as compared with the uniform TPMS-filled components. However, the current mechanical performance of the conformal lattice is not optimized. For future research, by optimizing the relative density and the orientation distributions of the conformal lattices, the optimal mechanical properties of the conformal TPMS components may be achieved.

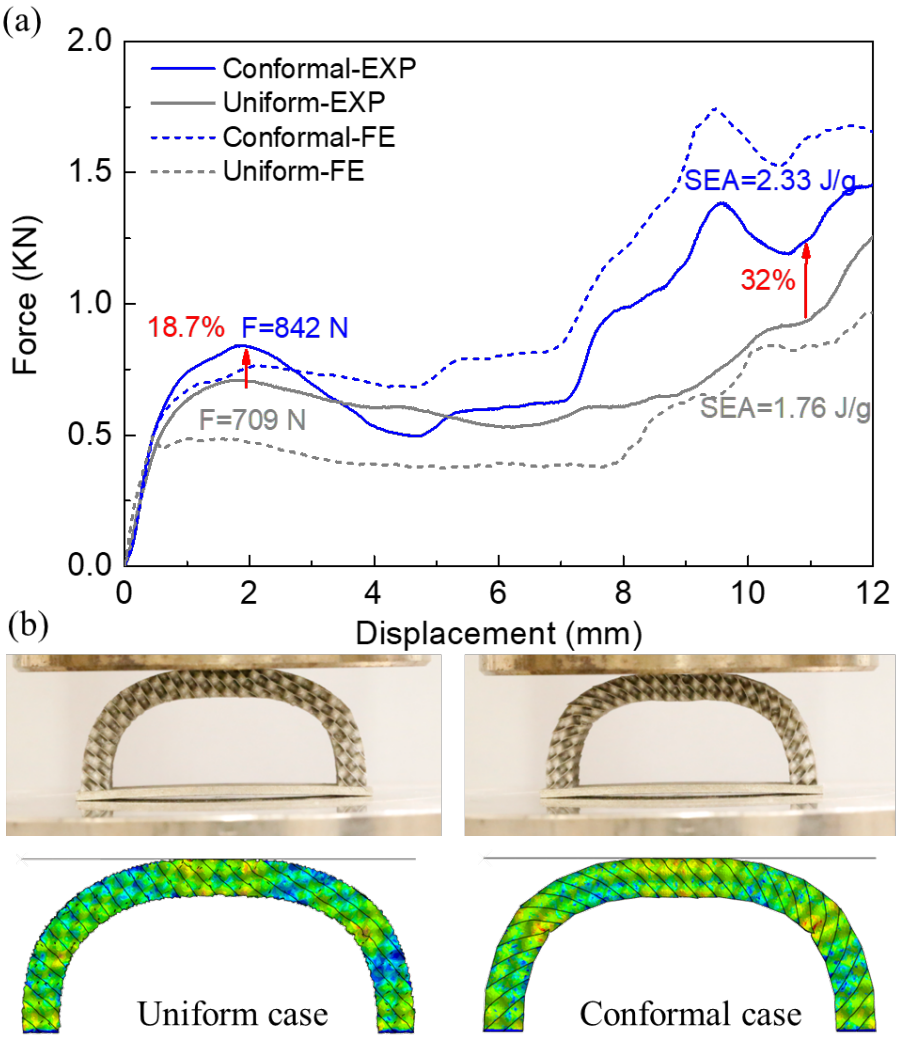

Fig. 12. (a) Numerical and (b) experimental load-displacement curves of the conformal and the uniform TPMS-filled monoclastic lattices; (c) simulated stress distribution and experimental deformation pattern of the lattices at the displacement of 3 mm. The color plots show the von Mises stress with the same color bar as shown in Fig. 6.

Table 3. Mechanical properties of the conformal and uniform TPMS-filled monoclastic lattices.

	Conformal case		Uniform case	
	FE	EXP	FE	EXP
Mass (g)	2.59	4.35±0.06	2.59	4.59±0.07
RD (%)	6	10.2±0.31	6	10.8±0.34
$F_{initial}$ (N)	766.08	842.26	493.20	709.59
W (J)	11.97	10.15	6.05	8.06
SEA (J/g)	4.62	2.33	2.34	1.76
F_{max} (N)	1746.15	1454.28	967.63	1258.86
F_{av} (N)	997.50	845.83	504.17	671.67
η (%)	57.13	58.16	52.10	53.36

4. Conclusions

In this research, the design method of TPMS-based conformal lattices was implemented based on isoparametric transformation. The roles of key design factors, including unit cell orientation, shape transformation and connection between cells, on the mechanical properties of conformal structures were evaluated by finite element modeling and quasi-static compression tests. Conformal TPMS-filled monoclastic lattice in terms of its crashworthiness was studied to verify the effectiveness of conformal lattice components for mechanical applications. The main findings are as follows:

(1) The deformation is highly influenced by the tilting angle of the side walls and the type of shape transformation, while the variation of cell orientation does not evidently change the deformation mode. With increasing tilting angle, the deformation is more likely to be layer-by-layer collapse of the horizontal layers from top to bottom. The tilting of the side walls could lead to a gradient distribution of local relative density and load bearing capacity, which allows the specimen to deform like a functional gradient lattice structure.

(2) The mechanical properties and the energy absorption capability of the shape-transformed and jointed TPMS specimens are determined by the tilting angle, shape transformation type and cell orientation. The overall mechanical properties are decreased with the

increasing tilting angle. The transformed TPMS maintains the anisotropy of mechanical properties compared with the regular TPMS. The boundary between the jointed shape-transformed TPMS does not deteriorate the mechanical properties.

(3) Design of the dedicated conformal TPMS components needs to consider the appropriate tilting angle, the suitable shape transformation type and the optimal cell orientation, in such a way to obtain the desired mechanical properties. When sufficient initial strength is required by conformal structures, large tilting angle should be avoided, and [100] orientation for Diamond-type TPMS is preferred for conformal mapping compared with [110] and [111] orientations.

(4) In the case study of the conformal TPMS-filled monoclastic lattices, the conformal case presents a better mechanical performance with the higher values of the initial peak force, specific energy absorption and crushing efficiency, etc. The specific energy absorption (SEA) of the conformal one is even 32% higher than that of the uniform one. Both numerical and experimental results suggest an obvious geometric superiority of the conformal design over the uniform case. It highlights the potential of conformal design.

(5) The quantified relationship between the design factors and the various mechanical properties of the conformal structures forms the guideline to design the conformal TPMS components by tailoring design factors for lightweight and impact-protection applications. By feedback of the FE predicting errors into the up-front design decision making, it is feasible to design and manufacture the conformal TPMS components with the expected mechanical properties. In future research, the design guideline can also be combined with the topological optimization to design conformal TPMS components with the optimized volume fraction distribution and optimal properties.

Acknowledgements

The authors would like to thank GRF Project of 15228621 and Projects ZE1W and 1-CD4H from The Hong Kong Polytechnic University. SONG Xu would like to acknowledge the financial support from the project #RNE-p2-21 of the Shun Hing Institute of Advanced Engineering, The Chinese University of Hong Kong.

References

[1] A. du Plessis, C. Broeckhoven, I. Yadroitsava, I. Yadroitsev, C.H. Hands, R. Kunju, D. Bhate, Beautiful and Functional: A Review of Biomimetic Design in Additive Manufacturing,

Addit. Manuf. 27 (2019) 408-427.
[2] I. Manavitehrani, T.Y.L. Le, S. Daly, Y. Wang, P.K. Maitz, A. Schindeler, F. Dehghani, Formation of porous biodegradable scaffolds based on poly(propylene carbonate) using gas foaming technology, Mater. Sci. Eng., C 96 (2019) 824-830.
[3] X. Song, W. Zhai, R. Huang, J. Fu, M.W. Fu, F. Li, Metal-Based 3D-Printed Micro Parts & Structures, in: F.G. Caballero (Ed.), Encyclopedia of Materials: Metals and Allloys, Elsevier, Oxford, 2022, 448-461.
[4] J. Fu, Z. Hu, X. Song, W. Zhai, Y. Long, H. Li, M. Fu, Micro selective laser melting of NiTi shape memory alloy: Defects, microstructures and thermal/mechanical properties, Opt. Laser Technol. 131 (2020) 106374.
[5] S.C. Han, J.W. Lee, K. Kang, A New Type of Low Density Material: Shellular, Adv. Mater. 27 (2015) 5506-11.
[6] K. Wei, Q. Yang, X. Yang, Y. Tao, H. Xie, Z. Qu, D. Fang, Mechanical analysis and modeling of metallic lattice sandwich additively fabricated by selective laser melting, Thin-Walled Struct. 146 (2020).
[7] J.B. Berger, H.N.G. Wadley, R.M. Mcmeeking, Mechanical metamaterials at the theoretical limit of isotropic elastic stiffness, Nature 543 (2017) 533-537.
[8] C. Yan, L. Hao, A. Hussein, P. Young, D. Raymont, Advanced lightweight 316L stainless steel cellular lattice structures fabricated via selective laser melting, Mater. Des. 55 (2014) 533-541.
[9] A. Yánez, A. Herrera, O. Martel, D. Monopoli, H. Afonso, Compressive behaviour of gyroid lattice structures for human cancellous bone implant applications, Materials Science Engineering: C 68 (2016) 445-448.
[10] I. Maskery, N.T. Aboulkhair, A. Aremu, C. Tuck, I. Ashcroft, Compressive failure modes and energy absorption in additively manufactured double gyroid lattices, Addit. Manuf. 16 (2017) 24-29.
[11] S.N. Khaderi, V.S. Deshpande, N.A. Fleck, The stiffness and strength of the gyroid lattice, Int. J. Solids. Struct. 51 (2014) 3866-3877.
[12] M.R. Scherer, L. Li, P.M. Cunha, O.A. Scherman, U. Steiner, Enhanced Electrochromism in Gyroid-Structured Vanadium Pentoxide, Advanced Materials 24 (2012) 1217-1221.
[13] A.M. Abou-Ali, O. Al-Ketan, D.W. Lee, R. Rowshan, R.K. Abu Al-Rub, Mechanical behavior of polymeric selective laser sintered ligament and sheet based lattices of triply periodic minimal surface architectures, Mater. Des. 196 (2020) 109100.
[14] O. Al-Ketan, R. Rowshan, R.K. Abu Al-Rub, Topology-mechanical property relationship of 3D printed strut, skeletal, and sheet based periodic metallic cellular materials, Addit. Manuf. 19 (2018) 167-183.
[15] D.J. Yoo, Heterogeneous Porous Scaffold Design for Tissue Engineering Using Triply Periodic Minimal Surfaces, Int. J. Precis. Eng. Manuf. 13 (2012) 527-537.
[16] D.J. Yoo, Heterogeneous porous scaffold design using the continuous transformations of triply periodic minimal surface models, Int. J. Precis. Eng. Manuf. 14 (2013) 1743-1753.
[17] D.J. Yoo, Advanced Projection Image Generation Algorithm for Fabrication of a Tissue Scaffold using Volumetric Distance Field, Int. J. Precis. Eng. Manuf. 15 (2014) 2117-2126.
[18] D.J. Yoo, K.H. Kim, An advanced multi-morphology porous scaffold design method using volumetric distance field and beta growth function, Int. J. Precis. Eng. Manuf. 16 (2015)

2021-2032.
[19] A. Hadi, F. Vignat, F. Villeneuve, Design Configurations and Creation of Lattice Structures for Metallic Additive Manufacturing, 14ème Colloque National AIP PRIMECA, La Plagne, France, 2015.
[20] J. Kim, D.-J. Yoo, 3D printed compact heat exchangers with mathematically defined core structures, Journal of Computational Design and Engineering 7 (2020) 527-550.
[21] M. Zhao, B. Ji, D.Z. Zhang, H. Li, H. Zhou, Design and mechanical performances of a novel functionally graded sheet-based lattice structure, Addit. Manuf. 52 (2022).
[22] https://ntopology.com/.
[23] T. Blacker, Meeting the challenge for automated conformal hexahedral meshing, 9th international meshing roundtable, Citeseer, 2000, 11-20.
[24] C. Bonatti, D. Mohr, Smooth-shell metamaterials of cubic symmetry: Anisotropic elasticity, yield strength and specific energy absorption, Acta Mater. 164 (2019) 301-321.
[25] O. Al-Ketan, R. Rezgui, R. Rowshan, H.F. Du, N.X. Fang, R.K. Abu Al-Rub, Microarchitected stretching-dominated mechanical metamaterials with minimal surface topologies, Adv. Eng. Mater. 20 (2018) 1800029.
[26] L. Zhang, S. Feih, S. Daynes, S. Chang, M.Y. Wang, J. Wei, W.F. Lu, Energy absorption characteristics of metallic triply periodic minimal surface sheet structures under compressive loading, Addit. Manuf. 23 (2018) 505-515.
[27] J. Fu, J. Ding, S. Qu, L. Zhang, M.Y. Wang, M. Fu, X. Song, Improved light-weighting potential of SS316L triply periodic minimal surface shell lattices by micro laser powder bed fusion, Mater. Des. (2022) 111018.
[28] X. Guo, J. Ding, X. Li, S. Qu, X. Song, J.Y.H. Fuh, W.F. Lu, W. Zhai, Enhancement in the mechanical behaviour of a Schwarz Primitive periodic minimal surface lattice structure design, Int. J. Mech. Sci. 216 (2022) 106977.
[29] H. Yin, X. Zheng, G. Wen, C. Zhang, Z. Wu, Design optimization of a novel bio-inspired 3D porous structure for crashworthiness, Compos. Struct. 255 (2021) 112897.
[30] S. Qu, J. Ding, X. Song, Achieving Triply Periodic Minimal Surface Thin-Walled Structures by Micro Laser Powder Bed Fusion Process, Micromachines 12 (2021) 705.
[31] J. Fu, S. Qu, J. Ding, X. Song, M.W. Fu, Comparison of the microstructure, mechanical properties and distortion of stainless steel 316 L fabricated by micro and conventional laser powder bed fusion, Addit. Manuf. 44 (2021) 102067.
[32] Y. Wang, X. Ren, Z. Chen, Y. Jiang, X. Cao, S. Fang, T. Zhao, Y. Li, D. Fang, Numerical and experimental studies on compressive behavior of Gyroid lattice cylindrical shells, Mater. Des. 186 (2020) 108340.
[33] H. Yin, Z. Liu, J. Dai, G. Wen, C. Zhang, Crushing behavior and optimization of sheet-based 3D periodic cellular structures, Compos. B. Eng. 182 (2020) 107565.
[34] M. Benedetti, A. du Plessis, R.O. Ritchie, M. Dallago, S.M.J. Razavi, F. Berto, Architected cellular materials: A review on their mechanical properties towards fatigue-tolerant design and fabrication, Mater. Sci. Eng. R Rep. 144 (2021) 100606.
[35] T. Maconachie, M. Leary, B. Lozanovski, X.Z. Zhang, M. Qian, O. Faruque, M. Brandt, SLM lattice structures: Properties, performance, applications and challenges, Mater. Des. 183 (2019) 108137.
[36] L. Riva, P.S. Ginestra, E. Ceretti, Mechanical characterization and properties of

laser-based powder bed–fused lattice structures: a review, Int. J. Adv. Manuf. Technol. 113 (2021) 649-671.
[37] C. Bhat, A. Kumar, S.-C. Lin, J.-Y. Jeng, A novel bioinspired architectured materials with interlocking designs based on tessellation, Addit. Manuf. 58 (2022) 103052.
[38] H. Li, H.Q. Zhang, H. Yang, M.W. Fu, H. Yang, Anisotropic and asymmetrical yielding and its evolution in plastic deformation: Titanium tubular materials, Int. J. Plast. 90 (2017) 177-211.
[39] C. Zhang, Z. Jiang, L. Zhao, W. Guo, Z. Jiang, X. Li, G. Chen, Mechanical characteristics and deformation mechanism of functionally graded triply periodic minimal surface structures fabricated using stereolithography, Int. J. Mech. Sci. 208 (2021) 106679.
[40] M. Zhao, D.Z. Zhang, F. Liu, Z. Li, Z. Ma, Z. Ren, Mechanical and energy absorption characteristics of additively manufactured functionally graded sheet lattice structures with minimal surfaces, Int. J. Mech. Sci. 167 (2020) 105262.
[41] H.L. Zhou, M. Zhao, Z.B. Ma, D.Z. Zhang, G. Fu, Sheet and network based functionally graded lattice structures manufactured by selective laser melting: Design, mechanical properties, and simulation, Int. J. Mech. Sci. 175 (2020) 105480.
[42] O. Al-Ketan, D.W. Lee, R. Rowshan, R.K. Abu Al-Rub, Functionally graded and multi-morphology sheet TPMS lattices: Design, manufacturing, and mechanical properties, J Mech Behav Biomed Mater 102 (2020) 103520.
[43] F. Liu, Z. Mao, P. Zhang, D.Z. Zhang, J. Jiang, Z. Ma, Functionally graded porous scaffolds in multiple patterns: New design method, physical and mechanical properties, Mater. Des. 160 (2018) 849-860.
[44] S.X. Yu, J.X. Sun, J.M. Bai, Investigation of functionally graded TPMS structures fabricated by additive manufacturing, Mater. Des. 182 (2019) 108021.
[45] ISO 13314: 2011, Mechanical Testing of Metals-Ductility Testing-Compression Test for Porous and Cellular Metals, International Organization for Standardization, 2011.
[46] H. Yin, Y. Xiao, G. Wen, Q. Qing, X. Wu, Crushing analysis and multi-objective optimization design for bionic thin-walled structure, Mater. Des. 87 (2015) 825-834.
[47] J. Fu, H. Li, X. Song, M.W. Fu, Multi-scale defects in powder-based additively manufactured metals and alloys, J. Mater. Sci. Technol. 122 (2022) 165-199.
[48] S.M. Ahmadi, R. Kumar, E.V. Borisov, R. Petrov, S. Leeflang, Y. Li, N. Tümer, R. Huizenga, C. Ayas, A.A. Zadpoor, V.A. Popovich, From microstructural design to surface engineering: A tailored approach for improving fatigue life of additively manufactured meta-biomaterials, Acta Biomater. 83 (2019) 153-166.
[49] C. Yan, L. Hao, A. Hussein, P. Young, Ti-6Al-4V triply periodic minimal surface structures for bone implants fabricated via selective laser melting, J Mech Behav Biomed Mater 51 (2015) 61-73.